

SparseCEM and SparseACE for Hyperspectral Image Target Detection

Shuo Yang, Zhenwei Shi, *Member, IEEE*

Abstract

Due to the limitation of spatial resolution of hyperspectral sensors, in real hyperspectral remote sensing images, targets of interest usually occupy only a few pixels (or even sub-pixels). Under such circumstances, we hope that the output of the detection algorithm is sparse. However, the existing detection algorithms seldom restrict this sparsity. Among the developed detection algorithms, constrained energy minimization (CEM) and adaptive coherence/cosine estimator (ACE) are two famous and widely used algorithms. In this letter, based on the CEM and the ACE, we propose the novel sparse constrained energy minimization (SparseCEM) and sparse adaptive coherence/cosine estimator (SparseACE) using the ℓ_1 norm regularization term to restrict the output to be sparse. Furthermore, we convert our detection models to second-order cone program (SOCP) problems, which can be solved efficiently by using the interior point method. The experiments on two real hyperspectral images demonstrate the effectiveness of the proposed algorithms.

Index Terms

Hyperspectral image, target detection, sparse constrained energy minimization, sparse adaptive coherence/cosine estimator.

I. INTRODUCTION

Hyperspectral image target detection has received considerable attention. In a hyperspectral image, each pixel has a nearly continuous spectrum with dozens or hundreds of very narrow bands, and all pixels with the same spectral bands form two dimensional images [1].

Several detection algorithms [1]-[5] have been developed. Matched filter (MF) [1] and adaptive coherence/cosine estimator (ACE) [1] are two hypothesis test based detection algorithms. MF and ACE first formulate the target

The work was supported by the National Natural Science Foundation of China under the Grants 61273245 and 91120301, the 973 Program under the Grant 2010CB327904, the Program for New Century Excellent Talents in University of Ministry of Education of China under the Grant NCET-11-0775, the funding project of State Key Laboratory of Virtual Reality Technology and Systems, Beihang University under the Grant VR-2014-ZZ-02, and State Scholarship Fund, P.R. China.

Shuo Yang, Zhenwei Shi (Corresponding Author) are with Image Processing Center, School of Astronautics, Beihang University, Beijing 100191, P.R. China (E-mail: shuoyangbuaa@gmail.com, shizhenwei@buaa.edu.cn).

detection as binary hypothesis test problems and then use the likelihood ratio (LR) test and the generalized-likelihood ratio test (GLRT) to obtain the detectors [1]. The constrained energy minimization (CEM) [2] algorithm builds a finite impulse response (FIR) filter which minimizes the total output energy under the constraint that the filter's response to the spectral signature of the target is unity. The formulations of MF and CEM are very similar. In fact, if there is a mean removing procedure before the detection, MF and CEM are equivalent [1].

In real situations, the spatial resolution of the hyperspectral sensor is not very high. Thus, in real hyperspectral remote sensing images, targets of interest usually occupy only a few pixels or are even sub-pixel targets. Under such circumstances, we hope that the output of the target detection algorithm is sparse, which means the output should contain only a few non-zero values. In this letter, based on CEM and ACE, we propose two novel algorithms named sparse constrained energy minimization (SparseCEM) and sparse adaptive coherence/cosine estimator (SparseACE) which use ℓ_1 norm regularization terms to restrict the outputs to be sparse and formulate the target detection as convex optimization problems. We further reformulate our target detection models as second-order cone program (SOCP) [6] problems, which can be solved efficiently by using the interior point method [6], [7]. The experiments on two real hyperspectral images show that the SparseCEM and SparseACE perform better than the original CEM and ACE.

II. BRIEF INTRODUCTIONS TO CEM AND ACE

A pixel's spectrum of an N -pixel hyperspectral image with L bands can be represented by a vector as $\mathbf{x}(n) = [x_1(n), \dots, x_L(n)]^T$ ($n = 1, \dots, N$), where T denotes matrix transpose. All spectra of an N -pixel hyperspectral image can be arranged in a matrix form as $\mathbf{X} = [\mathbf{x}(1) \dots \mathbf{x}(N)]$. Let $\mathbf{d} = [d_1, \dots, d_L]^T$ represent the spectral signature of the target of interest. \mathbf{d} can be obtained from the spectral library. In the rest of this letter, we use \mathbf{x} and \mathbf{d} to represent the original pixel's spectrum and spectral signature of the target, respectively, while we use \mathbf{x}_0 and \mathbf{d}_0 to represent the mean removed pixel's spectrum and spectral signature of the target, respectively.

The CEM [2] in fact is an FIR filter. Let $\mathbf{w} = [w_1, \dots, w_L]^T$ denote the coefficients of the filter. The filter's output of the pixel $\mathbf{x}(n)$ is $y(n) = \mathbf{w}^T \mathbf{x}(n)$. The \mathbf{w} of CEM is obtained by minimizing the total output energy subject to the constraint that the filter's response to \mathbf{d} is 1. The coefficients \mathbf{w} found by CEM is:

$$\mathbf{w}_{\text{CEM}} = \frac{\hat{\mathbf{C}}^{-1} \mathbf{d}}{\mathbf{d}^T \hat{\mathbf{C}}^{-1} \mathbf{d}} \quad (1)$$

where $\hat{\mathbf{C}} = \frac{1}{N} \sum_{n=1}^N [\mathbf{x}(n) \mathbf{x}^T(n)]$ is the estimated correlation matrix. Thus, for the pixel $\mathbf{x}(n)$, the output of CEM is:

$$y_{\text{CEM}}(\mathbf{x}) = \mathbf{w}_{\text{CEM}}^T \mathbf{x} = \frac{\mathbf{d}^T \hat{\mathbf{C}}^{-1} \mathbf{x}}{\mathbf{d}^T \hat{\mathbf{C}}^{-1} \mathbf{d}} \quad (2)$$

For the pixel $\mathbf{x}(n)$, the output of ACE is:

$$y_{\text{ACE}}(\mathbf{x}) = \frac{(\mathbf{x}_0^T \hat{\mathbf{\Gamma}}^{-1} \mathbf{d}_0)^2}{\mathbf{x}_0^T \hat{\mathbf{\Gamma}}^{-1} \mathbf{x}_0 \mathbf{d}_0^T \hat{\mathbf{\Gamma}}^{-1} \mathbf{d}_0} \quad (3)$$

where $\hat{\mathbf{\Gamma}} = \frac{1}{N} \sum_{n=1}^N [\mathbf{x}_0(n) \mathbf{x}_0^T(n)]$ is the estimated covariance matrix.

We can see the geometric interpretations of CEM and ACE by using the whitening transform as follows [1]:

$$\tilde{\mathbf{x}} = \hat{\mathbf{\Gamma}}^{-\frac{1}{2}} \mathbf{x}_0 \quad \tilde{\mathbf{d}} = \hat{\mathbf{\Gamma}}^{-\frac{1}{2}} \mathbf{d}_0 \quad (4)$$

After the whitening transform, the estimated covariance matrix of whitened hyperspectral data equals the identity matrix [1]. If \mathbf{x}_0 and \mathbf{d}_0 are used, $\hat{\mathbf{C}}$ equals $\hat{\mathbf{\Gamma}}$. Then the CEM becomes:

$$y_{\text{CEM}}(\mathbf{x}) = \frac{\mathbf{d}_0^T \hat{\mathbf{\Gamma}}^{-1} \mathbf{x}_0}{\mathbf{d}_0^T \hat{\mathbf{\Gamma}}^{-1} \mathbf{d}_0} \quad (5)$$

In fact, at this time, CEM equals MF [1]. Using the whitening transform (4), we can rewrite (5) and (3) as [1]:

$$y_{\text{CEM}}(\mathbf{x}) = \frac{\tilde{\mathbf{d}}^T \tilde{\mathbf{x}}}{\|\tilde{\mathbf{d}}\|^2} \quad (6)$$

$$y_{\text{ACE}}(\mathbf{x}) = \frac{(\tilde{\mathbf{x}}^T \tilde{\mathbf{d}})^2}{\|\tilde{\mathbf{x}}\|^2 \|\tilde{\mathbf{d}}\|^2} = \cos^2 \theta \quad (7)$$

where θ is the spectral angle between $\tilde{\mathbf{x}}$ and $\tilde{\mathbf{d}}$.

In this letter, we consider CEM and ACE from a new perspective. Consider the following optimization problem:

$$\min_{\mathbf{w}} \mathbf{w}^T \mathbf{w} \quad \text{s.t.} \quad \mathbf{w}^T \tilde{\mathbf{d}} = 1 \quad (8)$$

The solution of (8) is $\mathbf{w}^* = \frac{\tilde{\mathbf{d}}}{\|\tilde{\mathbf{d}}\|^2}$. So, noting (6), the CEM can be obtained as:

$$y_{\text{CEM}}(\mathbf{x}) = \mathbf{w}^{*T} \tilde{\mathbf{x}} = \frac{\tilde{\mathbf{d}}^T \tilde{\mathbf{x}}}{\|\tilde{\mathbf{d}}\|^2} \quad (9)$$

From (7), we can see that the output of ACE is the cosine square of the spectral angle between the whitened test pixel's spectrum $\tilde{\mathbf{x}}$ and the whitened target's spectral signature $\tilde{\mathbf{d}}$ [1]. Since the solution of (8) $\mathbf{w}^* = \frac{\tilde{\mathbf{d}}}{\|\tilde{\mathbf{d}}\|^2}$ has the same direction as $\tilde{\mathbf{d}}$, the cosine square of the spectral angle between $\tilde{\mathbf{x}}$ and $\tilde{\mathbf{d}}$ is the same as the cosine square of the angle between $\tilde{\mathbf{x}}$ and \mathbf{w}^* . So, the ACE can be obtained as:

$$y_{\text{ACE}}(\mathbf{x}) = \frac{(\tilde{\mathbf{x}}^T \tilde{\mathbf{d}})^2}{\|\tilde{\mathbf{x}}\|^2 \|\tilde{\mathbf{d}}\|^2} = \left(\frac{\mathbf{w}^{*T} \tilde{\mathbf{x}}}{\|\mathbf{w}^*\| \|\tilde{\mathbf{x}}\|} \right)^2 = \|\tilde{\mathbf{d}}\|^2 \left(\frac{\mathbf{w}^{*T} \tilde{\mathbf{x}}}{\|\tilde{\mathbf{x}}\|} \right)^2 \quad (10)$$

For a given hyperspectral image, $\|\tilde{\mathbf{d}}\|^2$ is a constant, which does not influence the detection result. Thus, $\|\tilde{\mathbf{d}}\|^2$ can be omitted, and $\left(\frac{\mathbf{w}^{*T} \tilde{\mathbf{x}}}{\|\tilde{\mathbf{x}}\|} \right)^2$ has the equivalent detection result with the original ACE in (3) and (10). From (9) and (10), we can see that after getting the solution of the optimization problem (8), CEM and ACE can be obtained by using (9) and (10), respectively.

III. SPARSECEM AND SPARSEACE

A. Formulation

Due to the limitation of spatial resolution, in real hyperspectral remote sensing images, targets of interest, such as airplanes and vehicles, usually occupy only a few pixels and have a small population. Also, at some time, sub-pixel targets need to be detected. The CEM minimizes the total output energy subject to the constraint that the output of the spectral signature of the target is 1. Thus, the essence of CEM is suppressing the background pixels' outputs and restricting them to be near zero while keeping large outputs of target pixels. Since targets of interest usually

occupy only a few pixels, we propose the sparse constrained energy minimization (SparseCEM) which adds a sparsity regularization term to CEM to force the output (i.e., $\mathbf{w}^T \mathbf{X}$) to be sparse so that the outputs of background pixels can be further suppressed and restricted to be near zero. At the same time, we require that the target pixels have large outputs. We use the constraint $\mathbf{w}^T \mathbf{d} = 1$ to guarantee that the spectral signature of the target has a large output. So, the algorithm will only restrict the outputs of background pixels to be near zero, while keeping large outputs of target pixels. In this way, the output ranges of target pixels and background pixels will be far away from each other, and the targets and background can be well separated in the output.

The ℓ_1 norm can formulate the sparsity effectively [8]. In this letter, we use the ℓ_1 norm to formulate the sparsity. The proposed SparseCEM can be formulated as the following constrained optimization problem:

$$\min_{\mathbf{w}} \mathbf{w}^T \hat{\mathbf{C}} \mathbf{w} + \lambda \|\mathbf{w}^T \mathbf{X}\|_1 \quad \text{s.t. } \mathbf{w}^T \mathbf{d} = 1 \quad (11)$$

where $\|\cdot\|_1$ denotes the ℓ_1 norm, and $\|\mathbf{w}^T \mathbf{X}\|_1 = \sum_{n=1}^N |\mathbf{w}^T \mathbf{x}(n)|$. λ is a positive constant.

We can apply a similar idea to ACE. As mentioned above, we can obtain the ACE by solving the optimization problem (8) and using (10). Since $\left(\frac{\mathbf{w}^{*T} \tilde{\mathbf{x}}}{\|\tilde{\mathbf{x}}\|}\right)^2$ has the equivalent detection result with the original output of ACE in (3) and (10), we can add a sparsity regularization term to (8) to force $\frac{\mathbf{w}^{*T} \tilde{\mathbf{x}}}{\|\tilde{\mathbf{x}}\|}$ to be sparse. Again, the ℓ_1 norm is used to formulate the sparsity. The proposed sparse adaptive coherence/cosine estimator (SparseACE) can be formulated as:

$$\min_{\mathbf{w}} \mathbf{w}^T \mathbf{w} + \lambda \sum_{n=1}^N \left| \frac{\mathbf{w}^T \tilde{\mathbf{x}}(n)}{\|\tilde{\mathbf{x}}(n)\|} \right| \quad \text{s.t. } \mathbf{w}^T \tilde{\mathbf{d}} = 1 \quad (12)$$

Let $\mathbf{w}_{\text{SparseCEM}}$ and $\mathbf{w}_{\text{SparseACE}}$ represent the solutions of (11) and (12), respectively. The outputs of SparseCEM and SparseACE can be obtained as:

$$y_{\text{SparseCEM}}(\mathbf{x}) = \mathbf{w}_{\text{SparseCEM}}^T \mathbf{x} \quad (13)$$

$$y_{\text{SparseACE}}(\mathbf{x}) = \|\tilde{\mathbf{d}}\|^2 \left(\frac{\mathbf{w}_{\text{SparseACE}}^T \tilde{\mathbf{x}}}{\|\tilde{\mathbf{x}}\|} \right)^2 \quad (14)$$

We can set a threshold η , if $\mathbf{w}_{\text{SparseCEM}}^T \mathbf{x}(n) > \eta$, we determine that the target is present in this pixel; otherwise we determine that the target is absent in this pixel. For the SparseACE, a threshold can be set similarly.

B. SOCP Implementation

The optimization problems (11) and (12) have no closed form solutions and are hard to solve directly. Since the ℓ_1 norm is non-differentiable, we cannot directly solve (11) and (12) by using the gradient based optimization methods. However, in the following, we will show that (11) and (12) belong to second-order cone program (SOCP) problems which can be solved efficiently by using the interior point method.

The SOCP [6] is a kind of nonlinear convex optimization problem, and has the following standard form:

$$\begin{aligned} \min \quad & \mathbf{f}^T \mathbf{y} \\ \text{s.t.} \quad & \|\mathbf{A}_i \mathbf{y} + \mathbf{b}_i\| \leq \mathbf{c}_i^T \mathbf{y} + g_i \quad i = 1, \dots, M \end{aligned} \quad (15)$$

where $\mathbf{y} \in \mathbf{R}^m$ is the optimization variable. The parameters are $\mathbf{f} \in \mathbf{R}^m$, $\mathbf{A}_i \in \mathbf{R}^{(m_i-1) \times m}$, $\mathbf{b}_i \in \mathbf{R}^{m_i-1}$, $\mathbf{c}_i \in \mathbf{R}^m$, and $g_i \in \mathbf{R}$. $\|\cdot\|$ denotes the Euclidean norm. The constraint $\|\mathbf{A}_i \mathbf{y} + \mathbf{b}_i\| \leq \mathbf{c}_i^T \mathbf{y} + g_i$ is called a second-order cone constraint of dimension m_i .

The detection model (11) equals the following convex optimization problem:

$$\min_{\mathbf{w}} \mathbf{w}^T \hat{\mathbf{C}} \mathbf{w} + \lambda \|\mathbf{w}^T \mathbf{X}\|_1 \quad \text{s.t.} \quad \mathbf{w}^T \mathbf{d} \geq 1 \quad (16)$$

because the optimal solution of (16) must be obtained when $\mathbf{w}^T \mathbf{d} = 1$ holds. We can see this as follows: for real hyperspectral images, the estimated correlation matrix $\hat{\mathbf{C}}$ is always positive definite, thus $\mathbf{w}^T \hat{\mathbf{C}} \mathbf{w}$ and $\|\mathbf{w}^T \mathbf{X}\|_1$ are all nonnegative. If $\mathbf{w}^T \mathbf{d} = a > 1$, we can decrease the objective function's value by replacing \mathbf{w} with \mathbf{w}/a which satisfies $(\mathbf{w}/a)^T \mathbf{d} = 1$. Noting that $\|\hat{\mathbf{C}}^{\frac{1}{2}} \mathbf{w}\|^2 = \mathbf{w}^T \hat{\mathbf{C}} \mathbf{w}$ and $\|\mathbf{w}^T \mathbf{X}\|_1 = \sum_{n=1}^N |\mathbf{x}^T(n) \mathbf{w}|$, (16) can be transformed to the following equivalent constrained optimization problem:

$$\begin{aligned} \min \quad & t_1 + \cdots + t_{N+1} \\ \text{s.t.} \quad & \lambda |\mathbf{x}^T(n) \mathbf{w}| \leq t_n \quad n = 1, \dots, N \\ & \|\hat{\mathbf{C}}^{\frac{1}{2}} \mathbf{w}\| \leq t_{N+1} \\ & 1 \leq \mathbf{d}^T \mathbf{w} \end{aligned} \quad (17)$$

Similarly, (12) can be transformed to the following equivalent constrained optimization problem:

$$\begin{aligned} \min \quad & t_1 + \cdots + t_{N+1} \\ \text{s.t.} \quad & \lambda |\tilde{\mathbf{x}}^T(n) \mathbf{w}| \leq \|\tilde{\mathbf{x}}(n)\| t_n \quad n = 1, \dots, N \\ & \|\mathbf{w}\| \leq t_{N+1} \\ & 1 \leq \tilde{\mathbf{d}}^T \mathbf{w} \end{aligned} \quad (18)$$

In (17) and (18), $\mathbf{w} \in \mathbf{R}^L$ and $t_j \in \mathbf{R}$ ($j = 1, \dots, N+1$) are optimization variables.

Comparing (17) and (18) with the SOCP's standard form (15), we can find (17) and (18) are SOCP problems. Next, we introduce a kind of interior point method named the "barrier method" [7] for solving the SOCP problems (17) and (18). Considering the following problems:

$$\begin{aligned} \min_{\mathbf{w}, t_j} f_1(\mathbf{w}, t_j) = s \sum_{j=1}^{N+1} t_j - \sum_{n=1}^N \log\{t_n^2 - [\lambda \mathbf{x}^T(n) \mathbf{w}]^2\} \\ - \log(t_{N+1}^2 - \mathbf{w}^T \hat{\mathbf{C}} \mathbf{w}) - \log(\mathbf{d}^T \mathbf{w} - 1) \end{aligned} \quad (19)$$

$$\begin{aligned} \min_{\mathbf{w}, t_j} f_2(\mathbf{w}, t_j) = s \sum_{j=1}^{N+1} t_j \\ - \sum_{n=1}^N \log\{t_n^2 \|\tilde{\mathbf{x}}(n)\|^2 - [\lambda \tilde{\mathbf{x}}^T(n) \mathbf{w}]^2\} \\ - \log(t_{N+1}^2 - \|\mathbf{w}\|^2) - \log(\tilde{\mathbf{d}}^T \mathbf{w} - 1) \end{aligned} \quad (20)$$

Algorithm 1 Barrier method for the SparseCEM and SparseACE

Initialization:1: Select strictly feasible \mathbf{z} of (17) or (18).Set $s > 0$, $\mu_1 > 1$, $0 < \mu_2 < 1$, tolerances $\epsilon_1 > 0$ and $\epsilon_2 > 0$.**Main iteration:****Subiteration (solve (19) or (20) by using Newton's method):**2: Use \mathbf{z} as the start point.3: Set $\mathbf{z}_{old} = \mathbf{z}$.4: Compute the gradient ∇f and the Hessian matrix $\nabla^2 f$ of f_1 or f_2 .5: Update $\mathbf{z} \leftarrow \mathbf{z} - \mu_2 \nabla^2 f^{-1} \nabla f$.**Stop subiteration** if $\|\mathbf{z} - \mathbf{z}_{old}\| < \epsilon_2$, and get $\mathbf{z}^*(s) = \mathbf{z}$;**else** go to step 3.**Stop main iteration** if $q/s < \epsilon_1$;**else** increase $s = \mu_1 s$, and go to step 2.

where $j = 1, \dots, N + 1$ and $s \in \mathbf{R}$, $s > 0$. Let $\mathbf{z} = [\mathbf{w}^T, t_1, \dots, t_{N+1}]^T$. Use $\mathbf{z}^*(s)$ to denote the solution of (19) or (20) with the parameter s , and use p^* to denote the optimal value of the original problem (17) or (18). It can be proved that [7]

$$f(\mathbf{z}^*(s)) - p^* \leq q/s \quad (21)$$

where q is the number of constraints in (17) or (18), and f denotes f_1 or f_2 . Thus, as $s \rightarrow \infty$, the solutions of (19) and (20) converge to the optimal points of the original problems (17) and (18), respectively. f_1 and f_2 are convex differentiable functions, and (19) and (20) can be solved by using Newton's method [7]. The basic idea of the barrier method is: increase s and solve the corresponding problems (19) and (20) repeatedly so that the solutions of (19) and (20) tend to the optimal points of the original problems (17) and (18) as s increases. Algorithm 1 gives the barrier method for the SparseCEM and SparseACE. Note that there are several efficient and robust software packages that can handle the SOCP problem. In this letter, we solve the SOCP problems by using the software package [9] for convenience.

IV. EXPERIMENT RESULTS AND DISCUSSION

In this section, two real hyperspectral images collected by the airborne visible/infrared imaging spectrometer (AVIRIS) and the hyperspectral mapper (HyMap) are used to conduct experiments. We compare the proposed SparseCEM and SparseACE with CEM and ACE. Receiver operating characteristic (ROC) curves [1] are used to compare algorithms. Based on ground truth, the ROC curve can plot the relationship between the false alarm rate and the probability of detection. The false alarm rate is defined as the ratio of the number of false alarm pixels to the number of total image pixels, and the probability of detection is defined as the ratio of the number of correct detection target pixels to the number of total true target pixels.

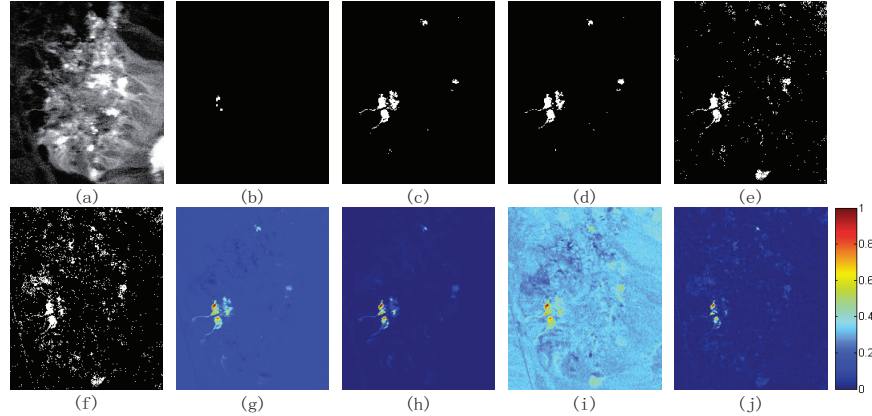


Fig. 1. (a) The first band of the AVIRIS hyperspectral image. (b) The ground truth of the buddingtonite target. Detection results for the AVIRIS hyperspectral image with (c) SparseCEM, (d) SparseACE, (e) CEM, and (f) ACE. The detection probabilities in (c)-(f) are all 0.5. Detection outputs for the AVIRIS hyperspectral image with (g) SparseCEM, (h) SparseACE, (i) CEM, and (j) ACE.

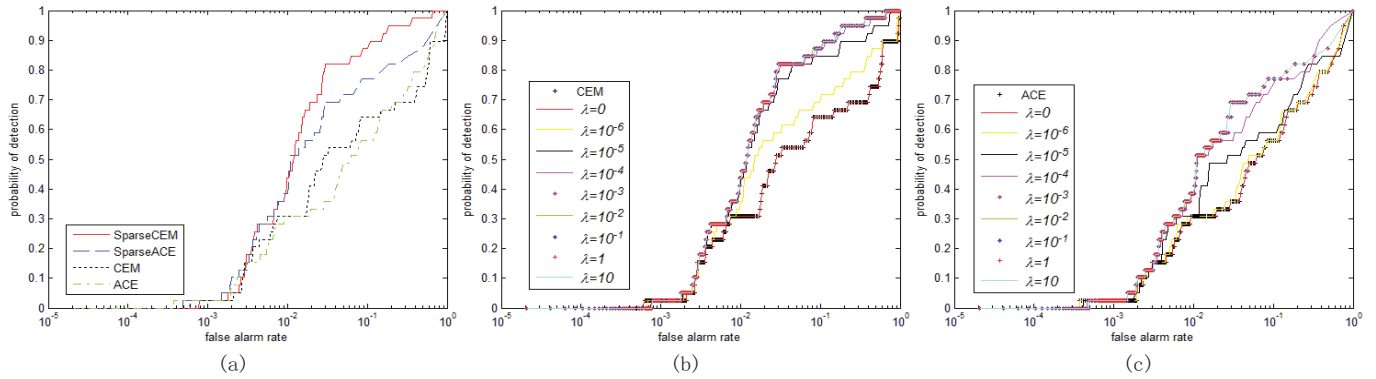


Fig. 2. (a) ROC curves of the experimental algorithms for the AVIRIS hyperspectral image. ROC curves of (b) SparseCEM and (c) SparseACE at different values of λ for the AVIRIS hyperspectral image.

A. Real Hyperspectral Image Experiment 1

In this subsection, we use an AVIRIS Cuprite hyperspectral image [10] to do experiments. AVIRIS collected hyperspectral data in 224 bands with the spectral range from 0.4 to 2.5 μm . The low signal-to-noise ratio (SNR) and water absorption bands have been removed from the experimental data, and 188 bands are left. Fig. 1(a) shows the first band of the AVIRIS hyperspectral image which has 250×191 pixels.

We use this AVIRIS hyperspectral image to detect the buddingtonite target. Fig. 1(b) shows the ground truth [11] of the buddingtonite target which in total has 39 pixels. The United States Geological Survey (USGS) Digital Spectral Library [12] has two spectra of the buddingtonite. We use the mean of these two spectra as the spectral signature of the target used in the experimental algorithms. λ s in the SparseCEM and SparseACE are both set to 1. Through setting suitable thresholds, the detection results of SparseCEM, SparseACE, CEM and ACE in the form of binary images are shown in Fig. 1(c)-(f) respectively. In Fig. 1(c)-(f), the detection probabilities of all

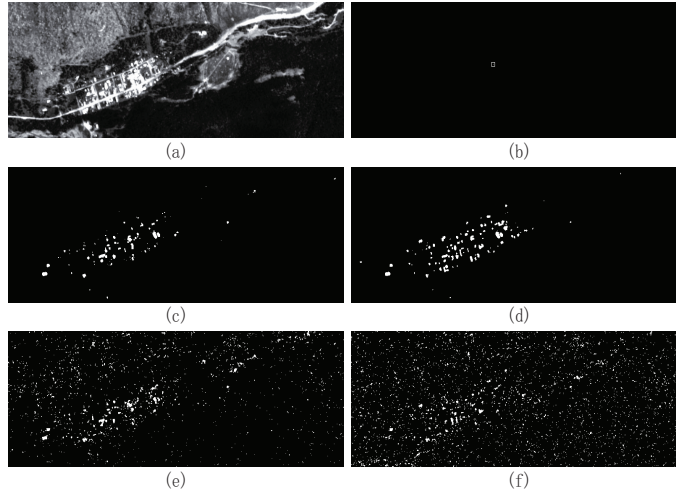


Fig. 3. (a) The first band of the HyMap self test set. (b) The ground truth of the V1 target in the self test set. Detection results for the V1 target of the HyMap self test set with (c) SparseCEM, (d) SparseACE, (e) CEM, and (f) ACE. The detection probabilities in (c)-(f) are all 1.

algorithms are all 0.5. From Fig. 1(c)-(f), we can see under the same detection probabilities, the false alarm pixels of SparseCEM and SparseACE are much fewer than the original CEM and ACE. Fig. 1(g)-(j) show the detection outputs of SparseCEM, SparseACE, CEM and ACE, respectively. The detection outputs have been normalized to $[0, 1]$. Fig. 1(g)-(j) show SparseCEM and SparseACE make the outputs sparser than the original CEM and ACE, respectively. From Fig. 1(g)-(j), we also can see SparseCEM and SparseACE make the target pixels' outputs more separable from the background pixels' outputs. The ROC curves plotted in Fig. 2(a) also verify that SparseCEM and SparseACE have better detection results.

B. Real Hyperspectral Image Experiment 2

The HyMap dataset in spectral reflectance after atmospheric compensation obtained from the Rochester Institute of Technology (RIT) Hyperspectral Target Detection Blind Test website [13] is used to evaluate the proposed algorithms. Both the self test set and the blind test set are used. The HyMap image has 126 bands with 280×800 pixels, and the spectral range is $0.45 - 2.5 \mu\text{m}$. The scene is the small town of Cooke City, Montana, USA. The first band of the HyMap self test set is shown in Fig. 3(a). The spectral signatures of targets used in the algorithms are also provided by the website. λ_s in SparseCEM and SparseACE are both set to 1.

In the HyMap dataset, there are three vehicle targets called V1, V2 and V3. We first use the self test set to detect the V1 target. The website provides the ground truth of targets in the self test set. The ground truth of V1 is shown in Fig. 3(b), where the bright point in the square is the location of V1. Since there is only one target pixel, the detection probability can only be 0 or 1. Through setting suitable thresholds, the detection results of V1 of SparseCEM, SparseACE, CEM and ACE in the form of binary images are shown in Fig. 3(c)-(f), respectively. In Fig. 3(c)-(f), the detection probabilities of all algorithms are all 1. From Fig. 3(c)-(f), we can clearly see that the false alarm pixels of SparseCEM and SparseACE are much fewer than the other experimental algorithms.

Next, we use the blind test set to detect the other two vehicle targets: V2 and V3. The website provides two distinctly different spectral signatures for V2, and we use the bed color one. Unlike the self test set, the website reserves the ground truth of the blind test set and does not provide it to the user. However, based on the reserved ground truth, the website provides an online application which can score the uploaded detection results. The score of an algorithm's detection result is the number of pixels whose detection outputs are equal to or larger than the target location pixel's detection output. A perfect score is one, which means the target pixel has the largest detection output. The score represents the number of false alarm pixels when the target is detected. The smaller the score is, the better the detection result is. We can use the score to calculate the false alarm rate. Table I gives the scores and false alarm rates (shown in parentheses) of different algorithms for V2 and V3. For the target V1 in the self test set, based on the provided ground truth, we calculate the scores and false alarm rates by ourselves, and also give them in Table I. From Table I, we can see that SparseCEM and SparseACE have much smaller scores and false alarm rates than the other experimental algorithms, thus have better detection results.

TABLE I
THE SCORES AND FALSE ALARM RATES OF DIFFERENT ALGORITHMS FOR THE HYMAP IMAGE

Target	SparseCEM	SparseACE	CEM	ACE
V1	1479(0.0066)	2286(0.0102)	5063(0.0226)	8065(0.0360)
V2	2497(0.0111)	1771(0.0079)	5215(0.0233)	17687(0.0790)
V3	2696(0.0120)	1661(0.0074)	3338(0.0149)	5637(0.0252)

C. Parameter Setting Analysis

Fig. 2(b) and Fig. 2(c) show ROC curves of SparseCEM and SparseACE at different values of λ for the AVIRIS dataset, respectively. The ROC curves of CEM and ACE are also plotted in Fig. 2(b) and Fig. 2(c), respectively. Fig. 2(b) and Fig. 2(c) show that the ROC curves of $\lambda = 0$ for SparseCEM and SparseACE are overlapped with CEM and ACE, respectively. This is because if λ s are set to 0, the SparseCEM equals CEM and the SparseACE equals ACE. For the SparseCEM, ROC curves of $\lambda = 10^{-3}$, $\lambda = 10^{-2}$, $\lambda = 10^{-1}$, $\lambda = 1$ and $\lambda = 10$ are overlapped and reflect better results than the other ROC curves. The worst result is obtained when λ is set to 0. For the SparseACE, ROC curves of $\lambda = 10^{-3}$, $\lambda = 10^{-2}$, $\lambda = 10^{-1}$, $\lambda = 1$ and $\lambda = 10$ are overlapped and intersect the ROC curve of $\lambda = 10^{-4}$. The worst result is also obtained when λ is set to 0. These results validate that the sparsity regularization terms can indeed improve the detection results. The SparseCEM and SparseACE are insensitive to the choices of λ in large ranges, because ROC curves are overlapped in large ranges of λ . This insensitivity is caused by the fact that the ℓ_1 norm regularization terms can restrict the background pixels' outputs to be near zero, and at the same time the constraints about the spectral signature of the target can guarantee that the target pixels' outputs are large. Thus, the constraints can guarantee that the proposed algorithms will not reduce the number of correct detection target pixels in the outputs.

V. CONCLUSION

Based on CEM and ACE, we propose the SparseCEM and SparseACE to restrict the outputs to be sparse. Furthermore, we reformulate the proposed detection models as SOCP problems. The experiments on two real hyperspectral images demonstrate the effectiveness of our proposed algorithms.

REFERENCES

- [1] D. Manolakis, D. Marden, and G. A. Shaw, "Hyperspectral image processing for automatic target detection applications," *Lincoln Lab. J.*, vol. 14, no. 1, pp. 79-116, 2003.
- [2] J. C. Harsanyi, Detection and classification of subpixel spectral signatures in hyperspectral image sequences, Ph.D. dissertation, University of Maryland Baltimore County, 1993.
- [3] B. Du and L. Zhang, "Target detection based on a dynamic subspace," *Pattern Recogn.*, vol. 47, no. 1, pp. 344-358, 2014.
- [4] Y. Zhang, B. Du, and L. Zhang, "Regularization framework for target detection in hyperspectral imagery," *IEEE Geosci. Remote Sens. Lett.*, vol. 11, no. 1, pp. 313-317, 2014.
- [5] L. Zhang, L. Zhang, D. Tao, and X. Huang, "Sparse transfer manifold embedding for hyperspectral target detection," *IEEE Trans. Geosci. Remote Sens.*, vol. 52, no. 2, pp. 1030-1043, Feb. 2014.
- [6] M. S. Lobo, L. Vandenberghe, S. Boyd, and H. Lebert, "Applications of second-order cone programming," *Linear Algebra Its Appl.*, vol. 284, no. 1-3, pp. 193-228, Nov. 1998.
- [7] S. Boyd and L. Vandenberghe, *Convex Optimization*. Cambridge, U.K.: Cambridge Univ. Press, 2004.
- [8] J. A. Tropp and S. J. Wright, "Computational methods for sparse solution of linear inverse problems," *Proceedings of the IEEE*, vol. 98, no. 6, pp. 948-958, 2010.
- [9] M. Grant and S. Boyd, *CVX: MATLAB software for disciplined convex programming*. [Online]. Available: <http://cvxr.com/cvx/>
- [10] AVIRIS Cuprite data set. [Online]. Available: <http://aviris.jpl.nasa.gov/html/aviris.freedata.html>
- [11] USGS map of the distribution of different minerals in the Cuprite mining district in Nevada. [Online]. Available: <http://speclab.cr.usgs.gov/PAPERS/tetracorder/>
- [12] R. N. Clark, G. A. Swayze, A. J. Gallagher, T. V. V. King, and W. M. Calvin, "The U.S. geological survey digital spectral library: Version 1: 0.2 to 3.0 microns," *U.S. Geological Survey, Denver, CO, Open File Rep.*, pp. 93-592, 1993.
- [13] D. Snyder, J. Kerekes, I. Fairweather, R. Crabtree, J. Shive, and S. Hager, "Development of a web-based application to evaluate target finding algorithms," in *Proc. IEEE Int. Geosci. Remote Sens. Symp.*, Boston, MA, United States, 2008, pp. II915-II918.